

Strain-rate dependent deformation mechanisms in single-layered Cu, Mo, and multilayer Cu/Mo thin films

Bibhu Prasad Sahu^{a*}, Wesley H. Higgins^b, Benjamin K Derby^c, George M. Pharr^b, Amit Misra^a

^a*Department of Materials Science and Engineering, University of Michigan, Ann Arbor, MI, 48109, USA*

^b*Department of Materials Science & Engineering, Texas A&M University, College Station, TX, 77843-3003 USA*

^c*Center for Integrated Nanotechnologies, Los Alamos National Laboratory, Los Alamos, NM 87545, USA*

* bpsahu@umich.edu, bibhu.igit@gmail.com

ABSTRACT

Strain-rate sensitivity and rate-dependent hardness, over a range of 10^{-2} to 10^2 s^{-1} , of sputter-deposited single-layered Cu, Mo, and 5 nm Cu/ 5 nm Mo, and 100 nm Cu/ 100 nm Mo multilayer films with a total film thickness of 5 μm were measured using nanoindentation. The plastic zone underneath the nanoindents was characterized via cross-sectional transmission electron microscopy (XTEM). The multilayer films exhibited enhanced hardness but slightly reduced strain-rate sensitivity with decreasing layer thickness from 100 nm to 5 nm. Only the 5 nm Cu/ 5 nm Mo multilayer film exhibited shear bands underneath the nanoindents, and the size of the shear bands increased with increasing strain rate. In contrast, the 100 nm Cu/ 100 nm Mo multilayer film exhibited material pile-up around the indents and significant nanotwinning within Cu grains. The effect of strain rate and layer thickness on the hardness and strain rate sensitivity of the multilayer thin films is interpreted using a modified confined layer slip (CLS) model. The reduced rate sensitivity at 5 nm as compared to 100 nm correlates with abundant growth nanotwins in the Cu grains in 100 nm and formation of shear bands in 5 nm multilayers. In single layer films, a substructure with a high density of dislocations was observed consistent with the plastic strain gradient in the indent plastic zone. No evidence of deformation twins was noted in any of the samples.

1. Introduction

Nanostructured multilayer films (NMFs) have been used as model systems to investigate length scale and interface effects in metal plasticity, primarily focused on low strain rates, $< \approx 10^{-2}$ /s, in a variety of metallic [1–6], metal-ceramic [7–10] and metal-metallic glass [11–14] systems. The effect of strain rate during nanoindentation testing on the deformation mechanisms of NMFs has not been investigated in detail, in comparison to studies of rate dependence in single-phase nanocrystalline metals [15–21].

The rate-dependent deformation in single-layered, and also NMFs, is usually evaluated by the strain-rate sensitivity, SRS (m), which offers valuable insight into the plastic deformation of the thin films by quantifying the response of the flow stress to the applied strain rate. Recent experimental observations suggest that m of nanocrystalline thin films is sensitive to grain size (d), film layer thickness (h), and nanotwin thickness (λ) below 100 nm [15–19]. Along with this, m is also observed to be sensitive to the crystal structure of the materials, such as face-centered cubic (fcc), body-centered cubic (bcc), or the hexagonal closed packed (hcp) metals [17,21–23]. Similar to the grain size in single-layered thin films, the layer thickness in NMFs affects the strain-rate sensitivity of the overall multilayer films. Carpenter *et al.* [24] revealed that the strain-rate sensitivity of multilayer 21 nm/21 nm Cu/Ni films is comparable to that of nanocrystalline fcc metals, and the value [$m=0.014$] increases with an increase in the strain during micropillar compression, which was attributed to the presence of underlying misfit dislocation structure of the Cu/Ni interfaces. The effect of nanolayer thickness on m was not reported. Similarly, using nanoindentation testing, Liu *et al.* [25] found that the SRS decreases with decreasing layer thickness below 10 nm for Cu/Ni multilayer films [$m=0.015$ in 10 nm NMF to $m=0.006$ for 1 nm NMF]. On the other hand, a decrease in the amorphous layer thickness from 225 nm to 90 nm in case of amorphous Cu-Zr-Al/nanocrystalline Cu nanolaminates leads to an increase in the SRS values from 0.021 to 0.034 during nanoindentation [26]. Further, it has been reported that incoherent interfaces in Cu/Ta multilayer films have an inverse influence on the SRS [$m=0.055$ in 60 nm NMF to $m=0.004$ for 30 nm NMF], i.e., increasing the number of interfaces leads to a decrease in the value of SRS because of activation event extension aided by an incoherent interface shear mechanism [27]. Moreover, Niu *et al.* [28] studied the size-dependent strengthening mechanisms and strain rate sensitivity of Cu/X (X = Cr, Zr) multilayer films demonstrating the influence of nanotwin formation during the film growth, as well as interface effects. This literature survey indicates a lack of a general

trend in the layer thickness-dependence of m of the multilayer films and thus the need to characterize deformation mechanisms over a range of strain rates and layer thickness to develop a better understanding of rate-dependent deformation mechanisms in nanolayered thin films.

Regarding the differences in the indentation rate-dependent deformation mechanisms in multilayer and single-layered films, several issues may arise such as: (a) an influence of the loading rate on the defect microstructure of the films, (b) effect of competitive deformation between the two constituent phases, (c) influence of interfaces on the strain-rate sensitivity, (d) the effect of individual layer thickness-dependence on m , and (e) characteristics of the specific as-deposited microstructure of the thin film, such as growth nanotwin formation. Considering these issues, the present investigation deals with the understanding of the difference in the deformation mechanism of single-layered films and thickness-dependent multilayer films. In this paper, we report a systematic investigation of the strain rate-dependent deformation mechanism in a range of loading strain rates (10^{-2} , 10^0 , and 10^2 s^{-1}) on sputter-deposited single-layered Cu, Mo, and multilayer 100 nm Cu/100 nm Mo, and 5 nm Cu/5 nm Mo films having a total thickness of 5 μm indented to a nominal depth of 500 nm. Further, in-depth microstructural characterization using cross-sectional transmission electron microscopy (XTEM) of the indentation response of the films at various strain rates has been carried out to understand the possible deformation mechanisms contributing to these effects. Special emphasis is given to the influence of individual layer thickness and the fraction of growth nanotwins on the flow stress and strain-rate sensitivity of the multilayer films by considering a modified confined layer dislocation slip model.

2. Experimental procedure

The single-layered Cu and single-layered Mo film, as well as the multilayer Cu 5 nm/Mo 5 nm and Cu 100 nm/Mo 100 nm films, were physical vapor deposited on thermally oxidized Si substrates at room temperature using DC magnetron sputtering (model: Kurt J Lesker PVD 75) at the University of Michigan. Two-inch Cu (99.999 % pure) and Mo (99.99 % pure) targets were held at 300 Watts during the deposition. To process the multilayer films, a target shutter was used to sequentially cover and uncover each target for the appropriate layer. The base pressure of the sputtering chamber was set at 1.07×10^{-5} Pa with a working pressure of 0.39 Pa of Argon. The total film thickness was 5 μm , and the deposition rates for Cu and Mo were 1.22 nm/s and 0.45 nm/s, respectively. The thermally oxidized substrates were pre-cleaned by applying a 30W bias on the substrate for 10 minutes

prior to deposition. The targets were oriented above the substrates in a “sputter-down,” off-axis configuration. The off-axis angle was approximately 30 degrees. Power was provided to each target with individual direct-current power supplies and power was constantly maintained throughout the deposition process.

Nanoindentation testing of the thin films was carried out at Texas A&M University using a commercially available nanoindenter from Nanomechanics Inc. equipped with an inForce 1000 actuator with a maximum force capability of 1 N and a standard diamond Berkovich tip. All indents made were kept to approximately 500 nm indentation depth by varying the maximum load to avoid substrate effects on the measured material response. The average value of hardness was estimated by considering a total of ten separate indent results. The experiments were conducted using constant indentation strain rate (CSR) conditions by keeping (\dot{P}/P) constant at 10^{-2} , 10^0 , and 10^2 s^{-1} . The applied strain rate during the loading is then given by

$$\dot{\epsilon} = \frac{\dot{P}}{2P}, \quad (1)$$

where P is the instantaneous load and $\dot{P} = dP/dt$ is the loading rate [29]. Further, the indentation hardness (H) of the specimens can be calculated using:

$$H = \frac{P}{24.56h^2}, \quad (2)$$

where, h is the contact depth. The strain-rate sensitivity index (m) is calculated as the slope of a log-log plot of the hardness-strain rate relation from

$$m = \frac{d \log H}{d \log \dot{\epsilon}}, \quad (3)$$

The transmission electron microscopy (TEM) as well as scanning S/TEM characterization of the as-deposited films and the indented films was conducted using a Thermo Fisher Talos F200X G2 S/TEM operated at 200 kV. The TEM specimens were prepared by focused ion beam milling (FIB) in a FEI Nova200 scanning electron microscope by lifting out from the indented region. A schematic representative image of the Berkovich indentation on the film highlighting the lift-out section cut for the TEM analysis is shown in supplementary document in Fig. S1. Detailed investigation of TEM specimen preparation by the FIB lift-out technique can be found in earlier literature by Bhattacharyya *et al.* [30]. For the single-layered films, the dislocation density (ρ) from the bright field TEM images was calculated using Ham’s random line interception method [31,32]:

$$\rho = \frac{2N}{Lt}, \quad (4)$$

where N is the number of intersections that dislocation lines make with a standard square grid, L is the total length of lines in a certain area covered by the grid and t is the thin foil thickness. t was measured using SEM during TEM sample preparation. For multilayer films, the reduction in layer thickness from TEM was used to estimate the true plastic strain along the indentation direction.

3. Results:

3.1. Strain rate dependent hardness measurement

Fig. 1(a) depicts the representative load vs displacement plots of the as-deposited films at a strain rate of 10^2 s^{-1} as obtained by nanoindentation testing. The data there confirm that the maximum depth reached for all the films during indentation is approximately 500 nm. Accordingly, the maximum load required to obtain a depth of 500 nm varied from $\approx 7.8 \text{ mN}$ for the single-layered Cu film, to $\approx 32 \text{ mN}$ for the single-layered Mo film, to $\approx 35 \text{ mN}$ for the 100 nm Cu/100 nm Mo film, and $\approx 40 \text{ mN}$ for the 5 nm Cu/5 nm Mo film. Fig. 1(b) presents plots of the indentation hardness against the loading strain rates for all the as-deposited single-layered and multilayer films. The hardness increases in the trend: single-layered Cu < single-layered Mo < 100 nm Cu/100 nm Mo < 5 nm Cu/5 nm Mo multilayer films. Further, it was observed that the hardness values of the films monotonically increase with an increase in the loading strain rates from 10^{-2} to 10^2 s^{-1} , which indicates positive values of the strain-rate sensitivity (m). The m values for the single-layered films of Cu and Mo were calculated as 0.015 ± 0.002 and 0.0207 ± 0.001 using Eq. (3). Interestingly, the m value of the 5 nm multilayer film was found to be 0.0186 ± 0.001 , which is slightly lower than that of 100 nm multilayer films (0.0206 ± 0.0009).

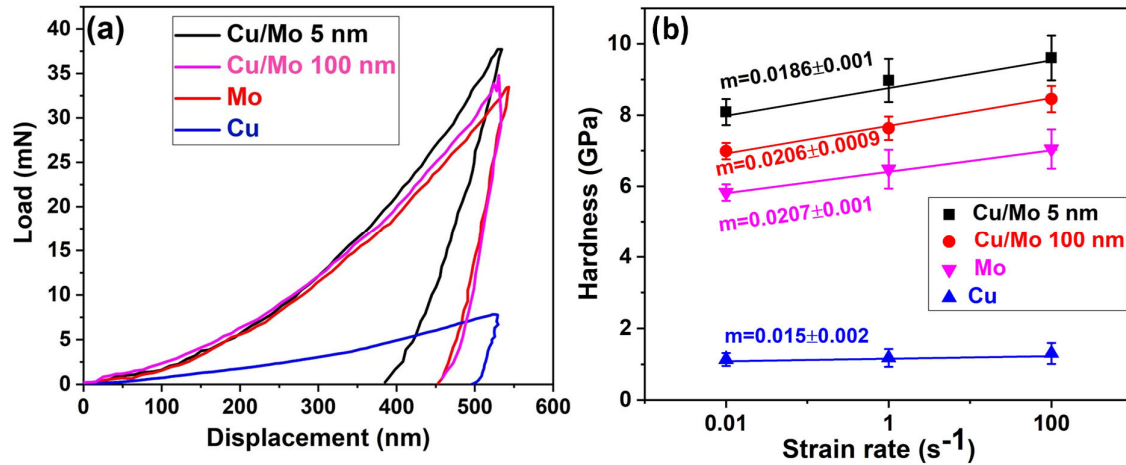


Fig. 1: (a) Typical load vs displacement plots for the as-deposited films at a loading strain rate of 10^2 s^{-1} condition, and (b) Hardness vs loading strain rate plots of the films. The slope of the log-log plot gives the corresponding strain-rate sensitivities (m).

3.2. Plan view SEM imaging of indents

Fig. 2 depicts the plan view SEM micrographs of the Berkovich indents on the films at 10^2 s^{-1} CSR condition. The impression of the Berkovich indent in the case of a pure single-layered Cu film is larger compared to the other films, confirming its lower value of hardness. Interestingly, a significant amount of material pile up was noticed in the case of Cu/Mo 100 nm multilayer films, which is found to be absent in the case of other films. A detailed analysis of relevant microstructural observations by TEM for all the films is described in the following sub-sections.

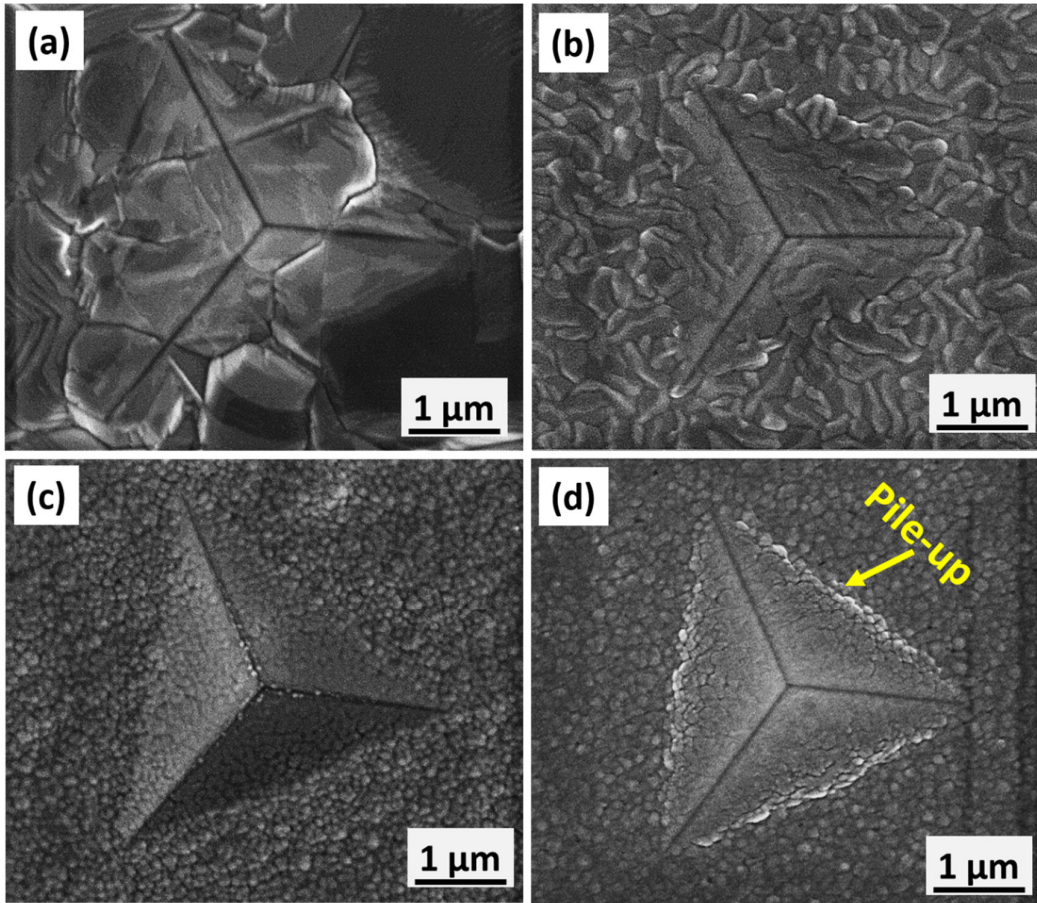


Fig. 2: SEM micrographs of the nominally 500 nm deep indent impressions in films of: (a) single-layered Cu, (b) single-layered Mo, (c) 5 nm Cu/5 nm Mo multilayer film, and (d) 100 nm Cu/100 nm Mo multilayer film.

3.3. TEM imaging of the as-deposited films

A bright field cross-section TEM image and the corresponding SAED pattern of the single-layered Cu film are shown in Figs. 3(a) and (b), respectively. The dashed yellow lines in the image mark the grain boundaries. The in-plane width of the grain ranges from 2 to 3 μm (Fig. 3(a)). The inset in the figure indicates the schematic view of the growth of the Cu grains during deposition. Further, the film contains numerous growth twins having a width of $\approx 230\text{-}300$ nm (specified by the red circles in Fig. 3(a)), formed during the sputter deposition. The presence of growth twins is consistent with the extra spots in the SAED pattern (Fig. 3(b)) taken from the small highlighted red circle in Fig. 3(a), which indicates that the twin has been formed parallel to the (111) planes of the Cu phase. Fig. 3(c) shows a cross-sectional TEM image of the as-deposited single-layer Mo film, whereas Fig. 3(d) indicates the corresponding diffraction pattern. Fig. 3(c) demonstrates a well-defined

columnar microstructure with uniform columns (in-plane width of each column having ≈ 150 - 200 nm) from the substrate to top of the films (a schematic view of the columnar growth perpendicular to the substrate surface is shown in the inset of Fig. 3(c)). A similar microstructure of the Mo film having a columnar growth perpendicular to the surface of the substrate has been reported previously [33,34].

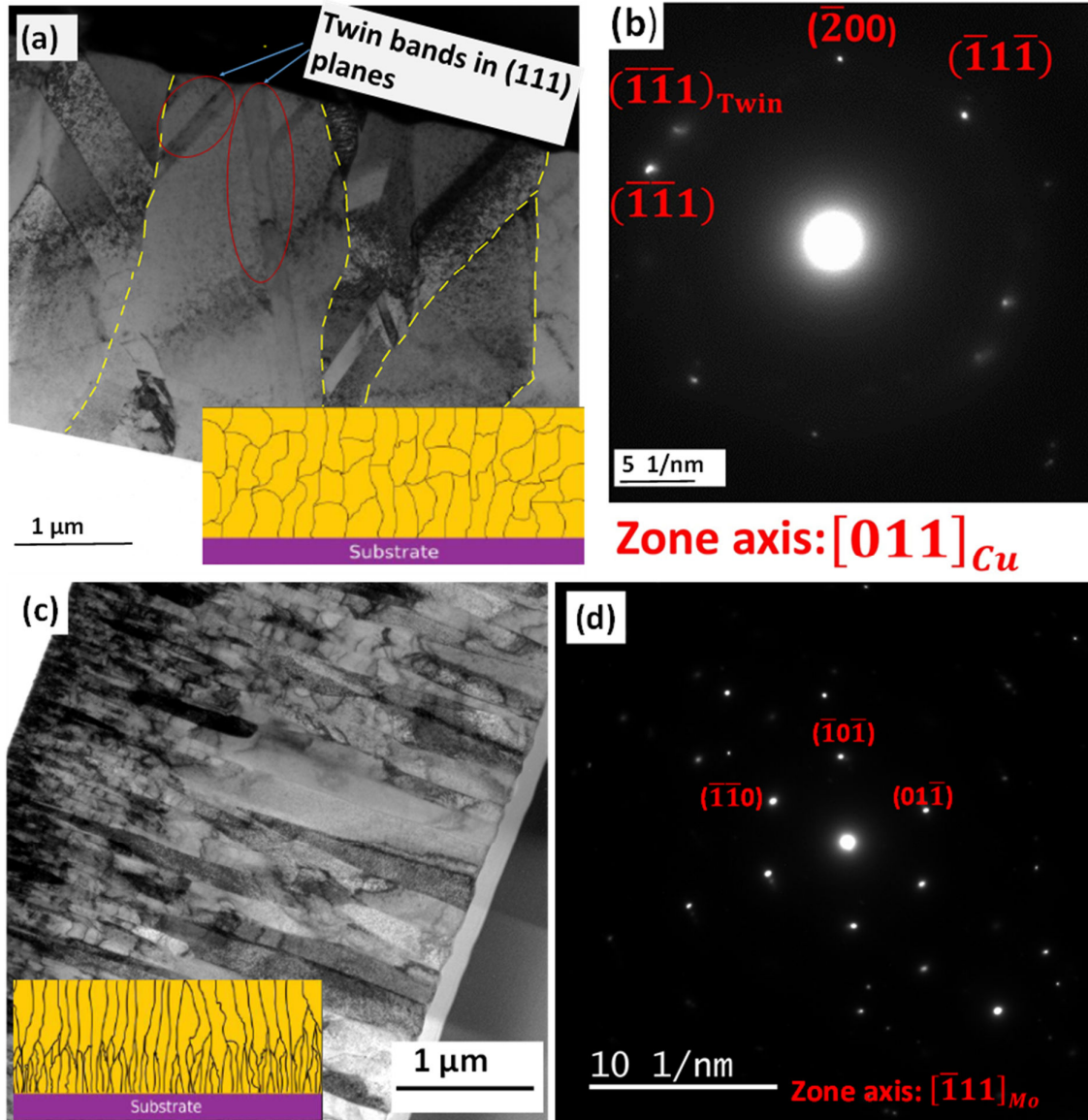


Fig. 3:(a) BF TEM image of the single-layered Cu film having the inset showing the schematic representation of the Cu growth, (b) SAED pattern of the single-layered Cu film from the small red circle of (a), (c) BF TEM image of the single-layered Mo film having the inset indicating the schematic representation of the columnar growth of Mo, and (d) SAED pattern of the single-layered Mo film from the encircled region of (c).

A typical cross-sectional STEM BF micrograph of the as-deposited 100 nm Cu/100 nm Mo multilayer film is shown in Fig. 4(a), which displays a clear multilayered structure with alternating Cu and Mo layers. The red arrow shown in Fig. 4(a) indicates the film growth direction. The diffraction pattern shown in Fig. 4(b) represents the nanocrystalline rings of the Cu and Mo phase having a weak $\{111\}\text{Cu} \parallel \{110\}\text{Mo}$ texture. The HAADF STEM image in Fig. 4(c) indicates that the Cu and the Mo phase appear dark and bright, respectively. The elemental STEM mapping of the film shown in the inset of Fig. 4(c) depicts the distribution of Cu and Mo. In addition, the Cu layers in the multilayer film show the appearance of nanotwins formed during the film growth (marked dotted circles in Fig. 4(a)). The twins have been formed either parallel to the interface (Fig. S2(a)) or in an inclined fashion (Fig. S2(b)). A HRTEM image focused mostly on the encircled region 1 of Fig. 4(a) is depicted in Fig. 4(d), which indicates that a growth nanotwin with thickness $\lambda \approx 7$ nm appears in the Cu phase parallel to (111) plane, as confirmed by the d-spacing ($d_{\text{Cu}(111)} = 2.08 \text{ \AA}$), whereas Fig. 4(e) represents the corresponding fast Fourier transform (FFT) indicating the twin pattern. The twins seem to orient at an angle of $\approx 70^\circ$ with the interface. In the 100 nm Cu/Mo multilayer film, the percentage of Cu grains containing nanotwins (N_T) is found to be $\approx 35\%$. A schematic representation of the 100 nm Cu/100 nm Mo multilayer film indicating the presence of growth twins oriented either in a parallel or in an inclined manner is shown in Fig. 4(f). The formation of such growth twins during sputter deposition has also been observed in previous studies [35,36].

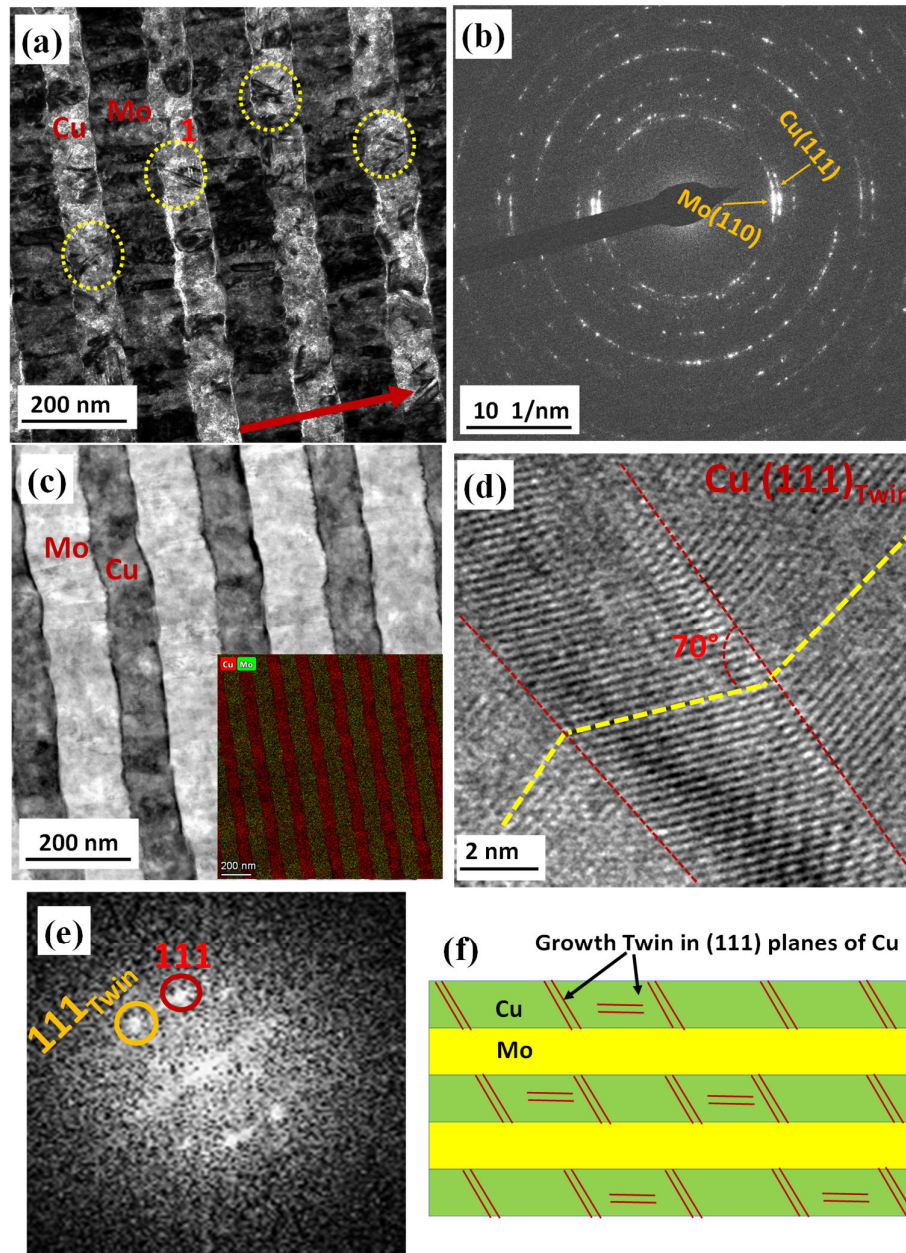


Fig. 4: Microstructure of the as-deposited Cu/Mo 100 nm multilayer film; (a) TEM BF micrograph showing the nanotwin, (b) corresponding diffraction pattern, (c) HAADF image including the STEM elemental mapping of Cu and Mo elements, (d) HRTEM image indicating the presence of growth nanotwin in Cu grains, (e) FFT of the twin pattern, and (f) schematic view of the Cu/Mo multilayer film with the twin formation. (Red arrow in Fig. (a) indicates the film growth direction)

The cross-sectional TEM BF, the corresponding diffraction pattern, and the HAADF STEM image of the 5 nm Cu/5 nm Mo multilayer film in the as-deposited condition are shown in Fig. 5. A columnar grain structure along with the waviness of the interface is

visible in Fig. 5(a), where the red arrow specifies the film growth direction. This is related to the island growth during deposition at room temperature which gives rise to the columnar grain structure. The diffraction pattern shown in Fig. 5(b) consists of rings representing the nanocrystalline grains of the Cu FCC phase and Mo BCC phase having a strong $\{111\}$ Cu || $\{110\}$ Mo fiber texture. The bright and the dark region of the HAADF image (Fig. 5(c)) represent the Mo and Cu phases, respectively. The average layer thickness of the film measured from Fig. 6(a) is ≈ 5.1 nm. The inset in Fig. 5(c) shows the STEM elemental mapping confirming the presence of Cu and Mo.

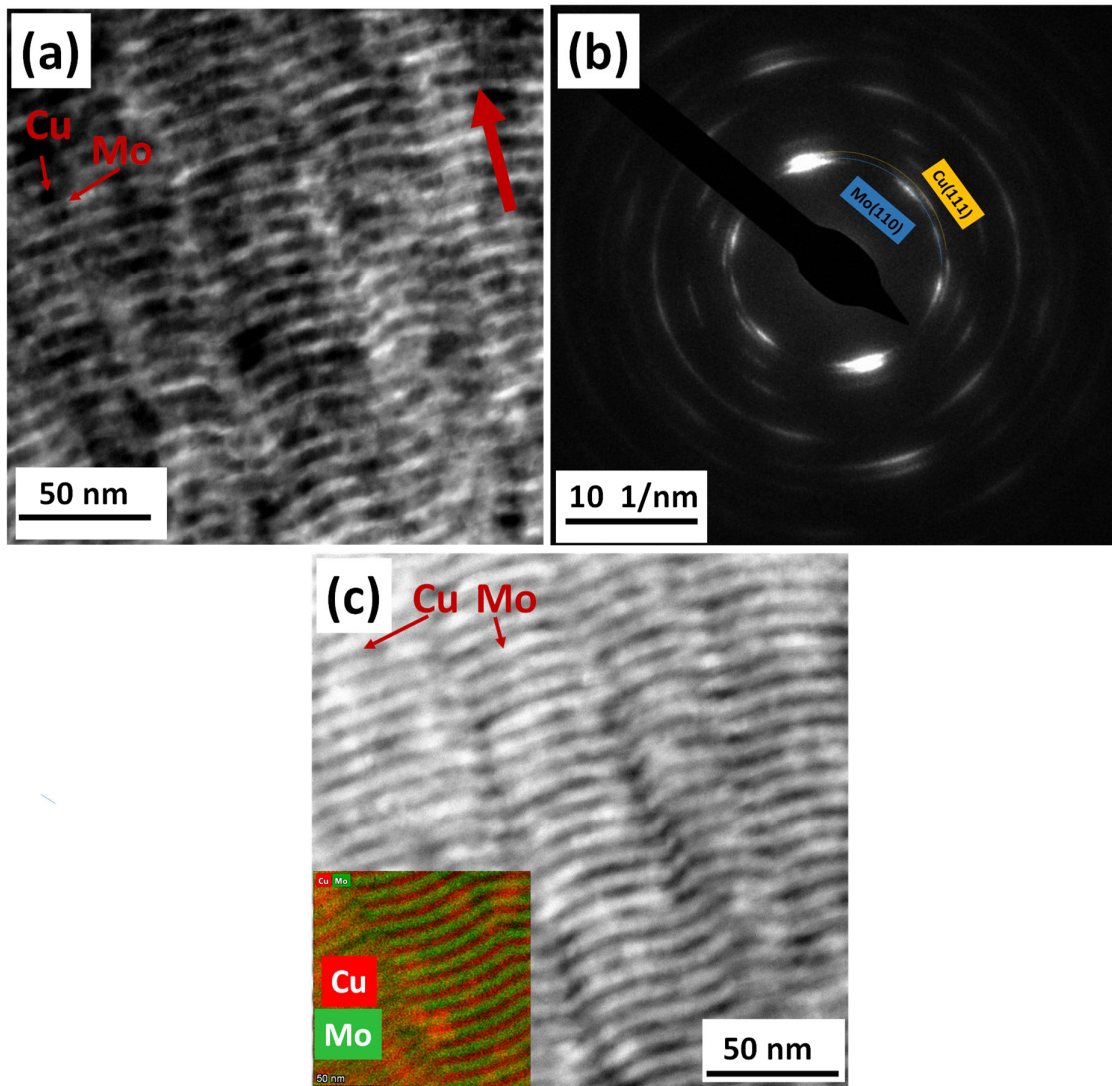


Fig. 5: Microstructures of the as-deposited Cu/Mo 5 nm multilayer film (a) TEM BF micrograph, (b) corresponding diffraction pattern showing the indicating the Cu(111) and Mo(110) phase, and (c) the HAADF STEM image, inset showing the STEM elemental mapping of Cu and Mo elements. (Red arrow in Fig. (a) indicates the film growth direction).

3.4. TEM imaging of the indented films

3.4.1. Single-layered films

Cross-sectional TEM was employed to investigate the evolution of the defect sub-structure in the single-layered Cu film at different indentation strain rates. Fig. 6 depicts the sub-structure of the Cu film deformed at 10^2 s^{-1} . The depth of the indent was measured to be approximately $\approx 510 \text{ nm}$, as mentioned in Fig. 6(a), which is about 10% of the total film thickness of $5 \mu\text{m}$. The indent impression seems to affect mostly three Cu grains specified by the dotted yellow lines in Fig. 6(a). A schematic representation of the indentation is shown in Fig. 6(b). It indicates that the top sections of the grains, G1, G2 and G3, are highly deformed by the indenter, such that the plastic zone extends $\approx 500 \text{ nm}$ from the indent surface. A magnified TEM image from the indented section covering two grains (G1 and G2) below the indenter is presented in Fig. 6(c). At a strain rate of 10^2 s^{-1} , several deformation characteristics are observed in the Cu grain (G1) close to the indented surface, as revealed in Fig. 6(c). The microstructure highlighted by the broken circle in Fig. 6(c) is shown in Fig. 6(d), which reveals a cell wall with a high-density of dislocations in the Cu grain (G1). Two square sections have been chosen to calculate the dislocation density of the Cu film using Eq. (4). Section 1 corresponds to a dislocation density (ρ) of $\approx 4.5 \times 10^{14} \text{ m}^{-2}$, whereas section 2 possesses a dislocation density (ρ) of $\approx 2.9 \times 10^{14} \text{ m}^{-2}$. Although the calculation of the dislocation density is not accurate, it provides qualitative information about the variation of the dislocation density with distance from the indentation. This result suggests that the density of dislocations decreases at a position away from the indent tip region, which is consistent with earlier observations [37]. Along with this, the interaction of dislocations with the neighboring grain boundary (G2) is also revealed, as indicated by the arrow in Fig. 6(d). Similar deformed microstructures were observed in case of other strain rates conditions.

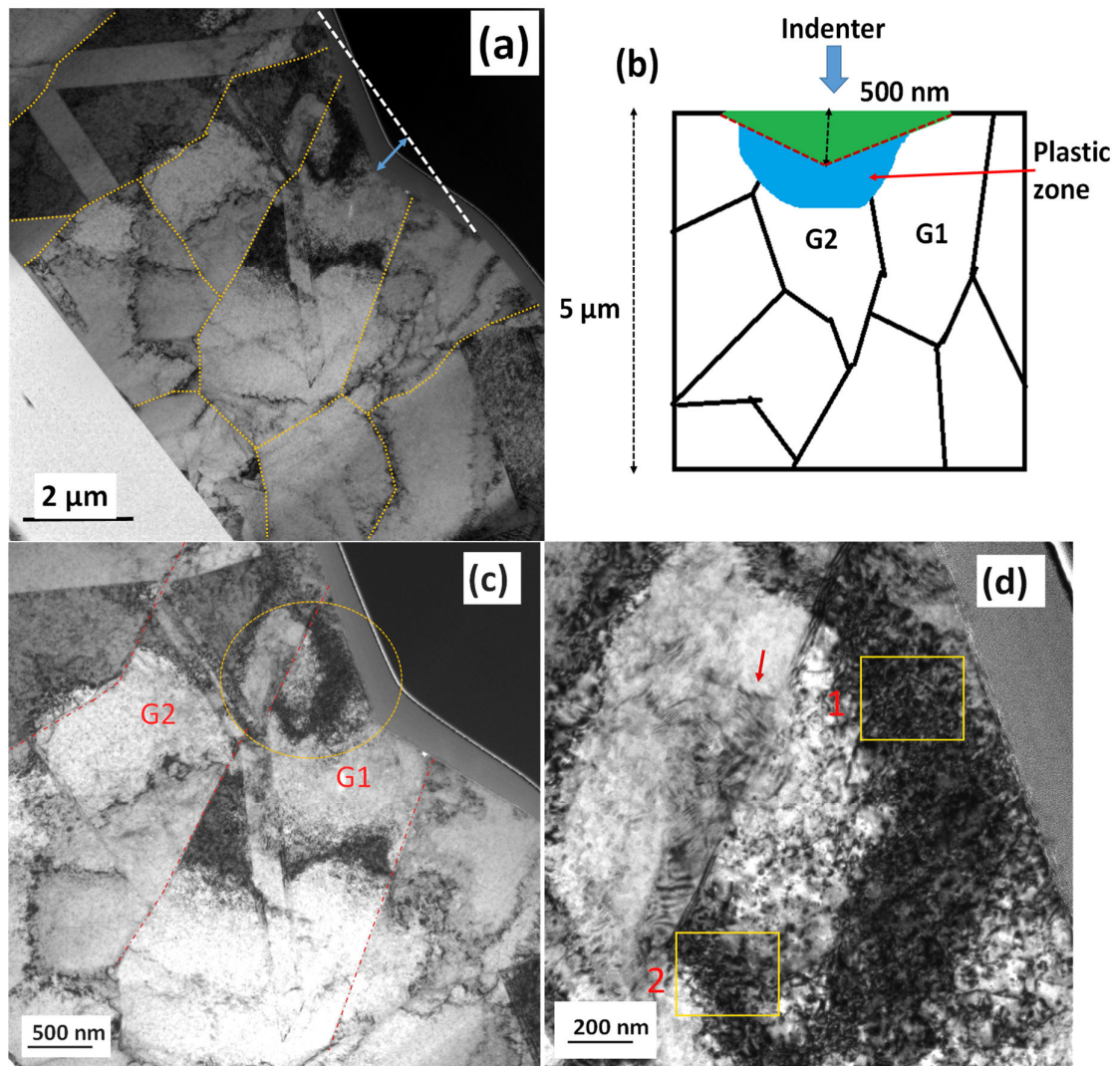


Fig. 6: TEM micrographs of the indented Cu films at a strain rate of 10^2 s^{-1} , (b) schematic view of the indent showing Cu grains, (c) magnified view of the indent region from two grains, G1 and G2, and (d) magnified view of the grain G1 highlighted by the broken circle in (c).

Fig. 7(a) depicts the cross-sectional TEM microstructure of the indented single-layered Mo film deformed at a strain rate of 10^2 s^{-1} . Interestingly, the top sections of the columnar grain (identified by the yellow broken lines) just beneath the indenter seem to be compressed to adjust to the shape of the indenter. The severity of the deformation decreases away from the indented surface suggesting the plastic zone extends to $\approx 700 \text{ nm}$ below the impression. An enlarged image near the indent is presented in Fig. 7(b). The figure shows that the columnar Mo grains seem to be severely deformed beneath the indenting tip up to a depth of $\approx 400 \text{ nm}$ (Fig. 7(b)), which is similar to that of single-layered

Cu film. The dislocation density has been calculated at the two square sections (1 and 2) as indicated in Fig. 7(b). Section 1 corresponds to a dislocation density (ρ) of $\approx 2.94 \times 10^{14} \text{ m}^{-2}$, whereas the section 2 possesses a dislocation density (ρ) of $\approx 1.48 \times 10^{14} \text{ m}^{-2}$. The deformed section immediately below the indenter tip demonstrates a clear evolution of the high density of dislocation network structure crossing the neighboring grains through grain boundary-dislocation interaction (indicated by the arrow in Fig. 7(b)).

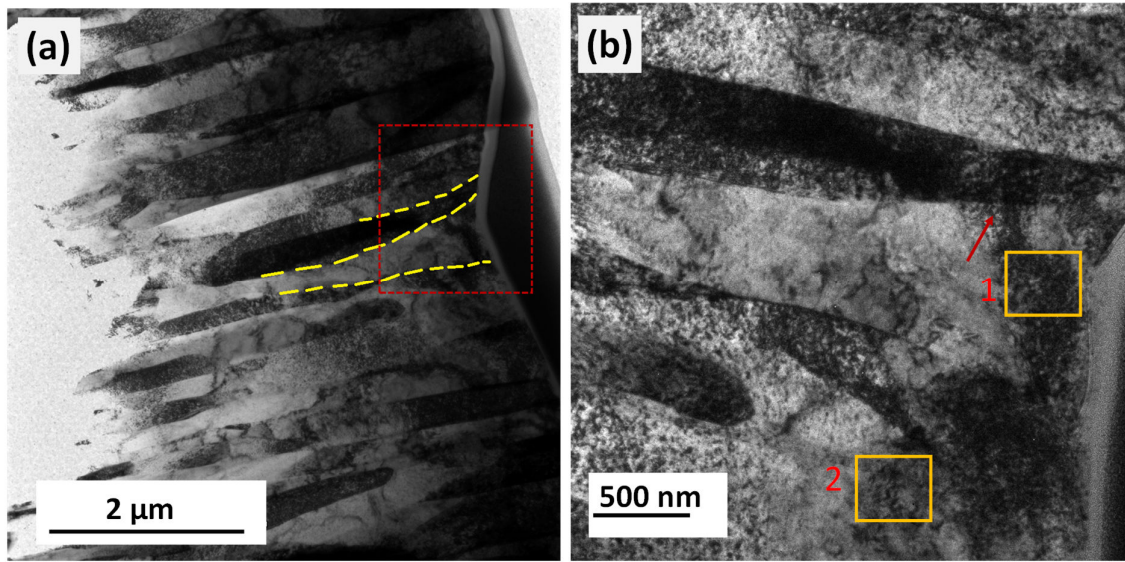


Fig. 7: (a) Cross-sectional BF TEM micrograph of the Mo film indented at a strain rate of 10^2 s^{-1} , and (b) magnified image adjacent to the indented region.

3.4.2. Cu/Mo multilayer films

The deformed microstructure of the 100 nm multilayer film after indentation at 10^2 s^{-1} strain rate condition is shown in Fig. 8. No shear bands are observed in the case of the deformed 100 nm Cu/Mo multilayer film, unlike the 5 nm deformed Cu/Mo multilayer film, which will be described later. The low magnification TEM image shows that the individual layers present immediately beneath the indent are severely bent and accordingly follow the shape of the indent up to $\approx 1 \text{ μm}$ depth below the indent, as shown in Fig. 8(a). Moreover, the magnified image of the indent section in Fig. 8(b) highlights that the individual layer thickness is found to decrease towards the indented surface, and that the very first layer seems to be significantly reduced to $\approx 33 \text{ nm}$ just below the tip of the indent. Therefore, by considering the reduction in layer thickness due to indentation, the plastic strain in the thickness direction can be considered as an important factor that explains the amount of deformation in both Cu and Mo layers. Fig. 8(c) represents the variation of the true

compressive plastic strain as a function of layer count (up to the fourth layer) from the indented surface. The plot for the Cu layer shows that the very first layer of Cu seems to be highly deformed by a significant reduction in the thickness to ≈ 33 nm and exhibiting a true plastic strain of 51.2 %. However, the true plastic strain value is found to decrease in subsequent Cu layers. Similarly, the plastic strain in case of Mo layers (Fig. 8(c)) is also found to decrease from 19.8 % in the first layer to 4.8% in the fourth layer. Interestingly, the section within the broken circle in Fig. 8(a), as magnified in Fig. 8(d), indicates that there is pile-up around the indent for the 100 nm multilayer film. This pile-up is mostly observed in the first layer of Cu, which is consistent with the aforementioned SEM result (Fig. 2(d)).

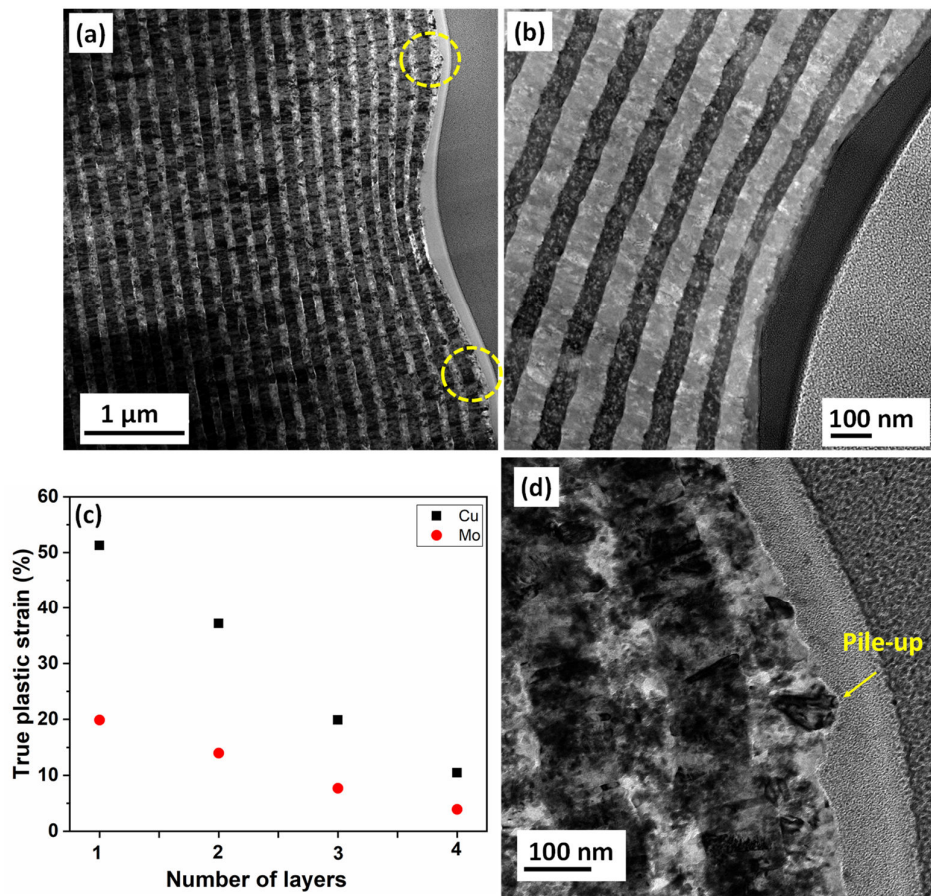


Fig. 8(a) BF TEM micrograph of the indent impression of the Cu/Mo 100 nm multilayer film at 10^2 s $^{-1}$ strain rate condition, and **(b)** A magnified HAADF STEM image of the indent region. **(c)** Plot of the maximum true compressive plastic strain against the number of layers from the indent surface for both Cu and Mo, and **(d)** the magnified image of the encircled region from **(a)** showing the pile-up.

Fig. 9(a) is a low magnification TEM image of the indent portion of the 5 nm Cu/5 nm Mo multilayer film after indentation at the 10^2 s^{-1} CSR condition. The magnified section in Fig. 9(b) clearly shows that the individual layers seem to be discontinuous and get highly deformed up to a depth of $\approx 100 \text{ nm}$ to 150 nm immediately beneath the indent. In comparison to the as-deposited film (Fig. 5(a)), Fig. 9 (b) indicates that the individual layer thickness of the deformed film gradually reduces towards the indented surface. Further, the highlighted region under the yellow square box shows a severely deformed zone. The SAED pattern collected from this region, shown in Fig. 9(c), is similar to that of the undeformed film. Interestingly, the corresponding HAADF image (Fig. 9 (d)) of the deformed zone was confirmed as a clear shear band, which originated from the indent tip, inclined at an angle of $\approx 40^\circ$ with the indented surface (indicated by the dashed yellow line) and extends up to a length of $\approx 180 \text{ nm}$. The enlarged image of the inclined shear band, Fig. 9(e), reveals that the individual layer thickness is significantly decreased, followed by subsequent bending of nanolayers inside the shear bands. To calculate the true compressive plastic strain parallel to the layer thickness, the individual layer thicknesses were measured at three locations [see the image shown Fig. 9(e) marked 1, 2, and 3] based on the distance from the shear bands. The thickness of the layers in locations 1, 2, and 3 were $\approx 4.4 \text{ nm}$, 3.2 nm , and 2.3 nm , respectively. As a result, the local strain parallel to the thickness direction is 11%, 30.7%, and 43.1% at locations 1, 2, and 3, respectively, which confirms that the deformed layers near the shear bands (i.e., at location 3) sustain large shear strains. In addition, the red dotted marks shown in Fig. 9(e) clearly depict that the subsequent layers inside the shear bands bend up to $\approx 20^\circ$ with respect to their orientations before entering into the shear bands. Such a formation of the shear bands immediately beneath the indent tip at a certain angle with the indented surface is in good agreement with the earlier reports [30,34]. Further, the layer interfaces gradually become unstable and cannot be observed inside the shear band. Fig. 9(f) depicts the HAADF STEM image of the deformed region of the Cu/Mo 5 nm multilayer film indented at a CSR of 10^{-2} s^{-1} . In this case, the length of the shear band that originated from the indented surface in an inclined fashion is measured to be quite smaller ($\approx 140 \text{ nm}$) than that of the shear band that emerged in the 10^2 s^{-1} condition. The thickness of the individual layers indented at 10^{-2} s^{-1} is also found to be reduced towards the indented surface. The thicknesses of the selected locations, 1, 2, and 3 are measured to be (marked in Fig. 9(f)) $\approx 4.7 \text{ nm}$, 3.8 nm , and 2.9 nm , respectively. Further, the true compressive local plastic strains parallel to the thickness direction are estimated to be 6%, 21.5%, and 35%, respectively, which are lower than those of the 10^2 s^{-1} strain rate condition.

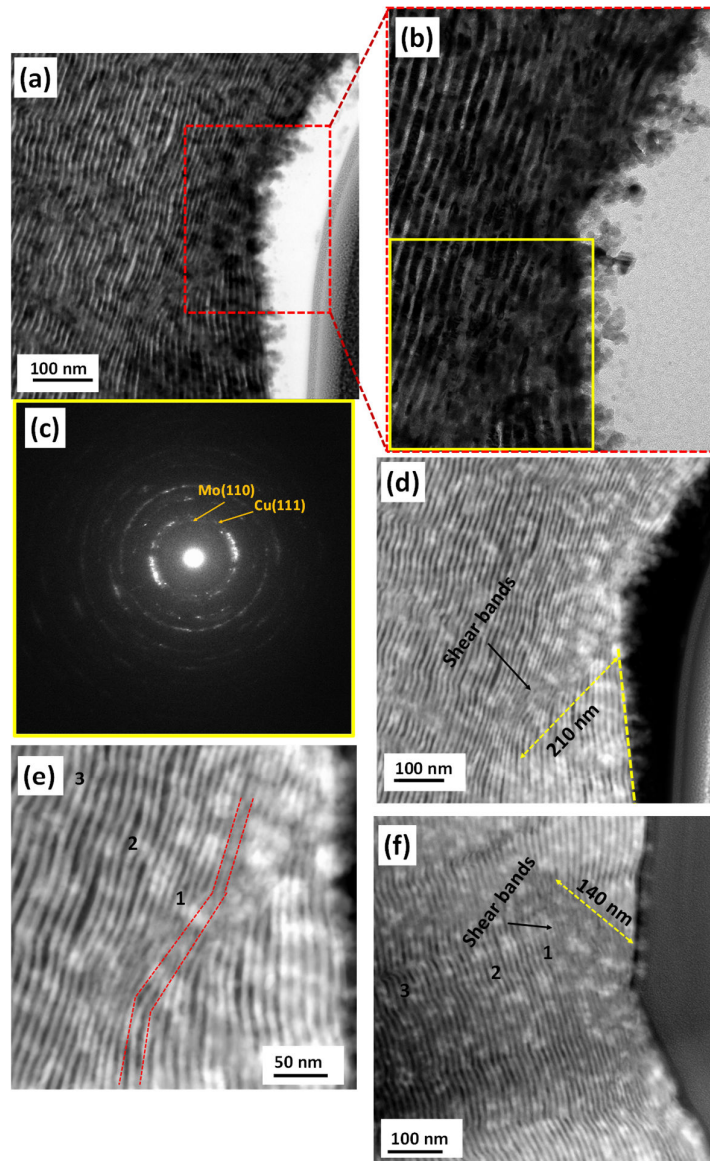


Fig. 9(a) STEM BF micrograph of the indent impression of the Cu/Mo 5 nm multilayer film at 10^2 s^{-1} strain rate condition, **(b)** Magnified TEM image from the marked region of Fig. (a), **(c)** the corresponding diffraction pattern from the highlighted yellow square in Fig. (b), **(d)** the STEM HAADF image, **(e)** magnified STEM HAADF from the shear bands, and **(f)** A HAADF STEM image of the indent region of the film deformed at 10^2 s^{-1} strain rate condition.

4. Discussion:

Based on the strain rate dependent nanoindentation tests and microstructural observations of the as-deposited and deformed films presented in the results section, here we discuss the strain rate sensitivity as well as the defect microstructures of the single-layered films beneath the indents on the basis of material type (Cu and Mo), grain size, and the effect of strain rate from 10^{-2} to 10^2 s^{-1} . For the multilayer films, we comment on the effect of layer

thickness on shear band formation, flow strength, and the SRS of the films. In particular, the size-dependent twin formation during deposition and its effect on the flow strength and the strain rate sensitivity of the multilayer films will be extensively analyzed by considering important interfacial effects. The size-dependent strengthening mechanisms of the multilayer films will be emphasized by comparing the experimental results with theoretical models focusing on the contribution of twin formation and layer thickness.

4.1. Single-layered films:

In case of the single-layered Cu film, the strain-rate sensitivity, m , was estimated to be 0.015 (Fig. 1(b)). Chen *et al.* have examined the SRS of the pure Cu in a range of grain sizes varying from coarse-grained to nanometer-scale (≈ 10 nm) and suggested that the m increases with decreasing the grain size [38]. Fig. 10 compares the variation of m from the present work with literature data as a function of grain size for pure Cu using various experimental techniques [17,39–43]. The agreement between the measured values of m with the literature in the micrometer range suggests that the nanoindentation technique employed has reasonable accuracy for determining rate sensitivity. Fig. 10 also confirms that the m values almost remain constant from macro to submicron scale, while a sudden rise is observed when the grain size is reduced below 100 nm. Such a variation in the trend of the m against the grain size is attributed to a transition in the deformation mechanism. Further, the m of the single-layered Mo film was estimated to be 0.027 (Fig. 1(b)), which is found to be higher than the values reported in nanocrystalline Mo thin films [44,45]. Earlier studies have reported that m for BCC metals with micrometer grain sizes is higher than for nano-sized grains [21,46]. It is apparent that in case of nanocrystalline fcc metals, GB-dislocation interactions serve as significant obstacles to dislocation motion, which enhance the m value. In contrast, the forest lattice dislocation mechanism within the grain dominates in micron-sized fcc metals, as is the case in the present study, thus resulting in a low value of m . The low value of m for the single-layered Cu film in the present investigation supports the fact that the microstructure evolved after indentation at various strain rates. Deformation studies on Cu [47] similarly show that the evolution of high density of dislocation cell structures is more prevalent with increasing the rate of deformation. The increased level of hardening response with increasing the strain rate or decreasing the temperature suggests that it is linked to both: (a) dislocation-dislocation interactions resulting from enhanced dislocation nucleation at the higher level of strain rate, and (b) suppression of dynamic recovery processes, which depend on cross-slip. However, in our case, as the hardness

doesn't vary much with the loading strain rates, and the resulting microstructures remain almost constant after indentation at various strain rate conditions.

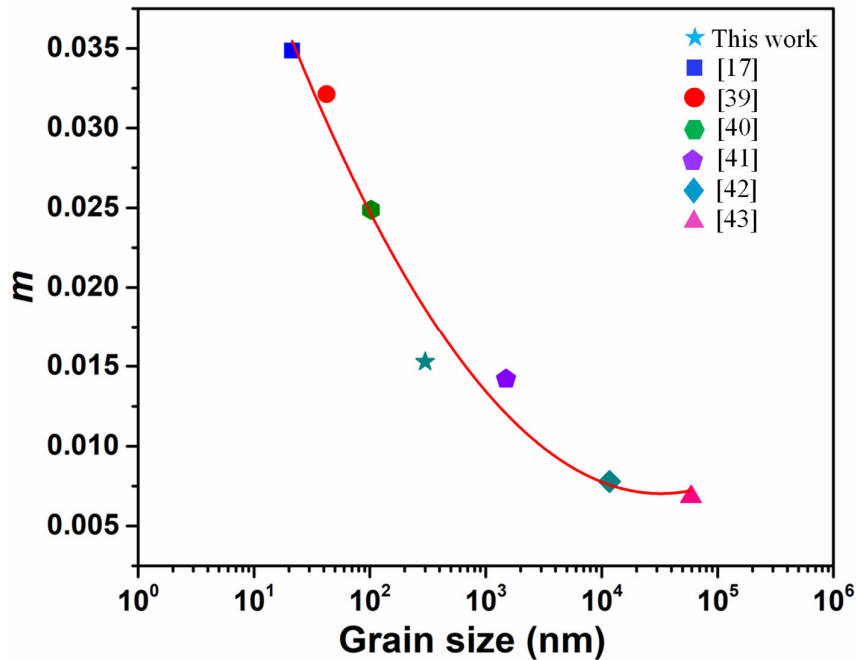


Fig. 10. The variation of m as a function of grain size for Cu using experimental data from the literature [17, 39, 40, 41, 42, 43] and from the present work.

4.2. Multilayer films:

The deformation mechanism in the multilayer films can be best explained by the variation in layer thickness. The absence of shear bands for the 100 nm multilayer film clearly indicates a different deformation mechanism from that of the 5 nm multilayer film, which contains a clear shear band emerging from the indent tip. The generalized Hall-Petch relation considering the pile-up of dislocations against grain boundaries is thus likely responsible for explaining the strengthening mechanism in case of the 100 nm multilayer film. The dislocations in the pile-up act cooperatively to overcome the interface barrier in order for the multilayers to yield. The larger the layer thickness, the more dislocations present in the pile-up and the softer the multilayers. Interestingly, by lowering the layer thickness below 20 nm, the dislocation activity decreases, which leads to a break-down of the Hall-Petch relationship [48]. Further, when reducing the layer thickness to a few tens of nanometers, the CLS mechanism [49] applies, which suggests that dislocation core spreading along the interface, interface stress, and interface dislocations on the confined layer increases the strength of the multilayer film with decreasing layer thickness.

Another interesting finding in the case of the 5 nm multilayer film is the evolution of shear bands during indentation. As explained by Cui *et al.* [34], at lower layer thicknesses, multiple dislocations glide through the interface forming shear bands, as indicated in Fig. 9(d) and (f). The region immediately beneath the indent undergoes severe stress concentration with the rotation of the layers, as long as the indenter is loaded into the multilayer. Therefore, the shearing along with the interface subsequently favors the interaction of slip on the interface by activating the shear bands. Further, the loading strain rate has also a major role in the deformation of the multilayer films. As reported by Xie *et al.* [50], the density, as well as size of shear bands, varies directly with the applied strain rate. In the present study, the size of the shear bands that emerged from the indented surface in the 10^2 s^{-1} strain rate condition was larger than that of the 10^{-2} s^{-1} strain rate condition (see Fig. 9(d) and (f)). At higher strain rates, plastic deformation in the soft phase (i.e. in the Cu layer) is high, generating higher stress concentrations in the hard phase (i.e. in the Mo layer). In this circumstance, deformation phenomena like grain boundary sliding, as well as grain rotation affect the orientation difference between the neighboring layers, such that a large number of shear bands are easily activated. The activation of a higher number of shear bands with larger size produces a large amount of plastic strain, which ultimately causes an increase in the hardness value.

Along with the shear band-mediated deformation mechanism in the 5 nm film, it is also expected that the growth nanotwins play a vital role in the deformation of the multilayer films. The present findings suggest that nanotwin formation decreases with decreasing layer thickness, which is similar to the experimental observation that the propensity of nanotwin formation decreases with either a decrease in grain size below 80 nm in NC Cu [51], or a decrease in the layer thickness in multilayer films [28]. It has been revealed that in nanocrystalline grains, not only the dislocation emission from GBs/interfaces and dislocation interaction with the neighboring GBs/interfaces affects the deformation mechanism, but twin boundaries (TBs) also affect the thermally activated processes via dislocation nucleation and interaction [19]. Interestingly, the reduction of the SRS with decreasing layer thickness observed in the present work is contrary to the general observation of enhanced m with reduced grain size in fcc NC materials [21,52]. Two possible reasons for this unusual trend include: (i) the influence of shear bands in the 5 nm multilayer films, and (ii) the influence of thickness-dependent nanotwin formation. Let us first consider the case regarding the influence of shear bands. It is well known that shear bands play an active role in the deformation of amorphous alloys [53]. Further, several studies have reported that activation of shear bands in metallic glasses gives rise to either a negative value of m or a reduced value, in contrast to their

crystalline counterparts [54–56]. Therefore, it can be expected that the emergence of shear bands from the indented surface in case of 5 nm multilayer films could contribute in reducing the m value to some extent.

As the nanotwin formation is specific to the Cu layers, we now discuss the size-dependent strengthening mechanism and the strain-rate sensitivity by analyzing the nanotwin formation in the Cu phase. Niu *et al.* [28] have extended the conventional CLS model [49] by incorporation of a the related to the twins as follows:

$$\sigma_{CLS} = \frac{M\mu^*b \sin \varphi}{8\pi h_{Cu}} \left(\frac{4-\nu}{1-\nu} \right) \ln \left(\frac{\alpha h_{Cu}}{b \sin \varphi} \right) + \frac{F}{h_{Cu}} + \frac{\mu^* f_{Mo} \varepsilon}{B(1-\nu)} + \frac{N_T}{100} k_T \lambda^{-1/2} \quad (5)$$

where, σ_{CLS} is the flow stress required to propagate a glide loop of Burgers vector, b confined to the Cu layer, M is the Taylor factor, φ is the angle between the slip plane and the interface, ν is the Poisson ratio of Cu, α is the core cut-off parameter, F represents the characteristic interface stress of the multilayer, ε is the in-plane plastic strain, and B is a strain resolution factor of the order of 0.5 for the active slip systems. $\mu^* = \frac{\mu_{Cu} \cdot \mu_{Mo}}{f_{Mo} \cdot \mu_{Cu} + f_{Cu} \cdot \mu_{Mo}}$ is the mean shear modulus of Cu/Mo multilayer films, which can be calculated from the shear modulus of Cu (μ_{Cu}), shear modulus of Mo (μ_{Mo}), and the volume fractions of Cu ($f_{Cu} = h_{Cu}/(h_{Mo} + h_{Cu})$) and Mo ($f_{Mo} = h_{Mo}/(h_{Mo} + h_{Cu})$). The second and third terms in Eq. (5) represent the contributions of the interface stress and the dislocation–dislocation interaction, respectively [49]. N_T and λ represent the percentage of Cu grains containing the nanotwin and the twin thickness in nm, respectively, which are mentioned in Table 1. As no evidence of growth of nanotwins was observed in case of the 5 nm multilayer film, the fourth term in Eq. 5 has been neglected for the calculation of the σ_{CLS} for the 5 nm multilayer film. By using $M = 3.06$, $\mu_{Cu} = 48.3$ GPa, $\mu_{Mo} = 118$ GPa, $\nu = 0.343$, $b = 0.2556$ nm, $\alpha = 0.2$, $F = 2$ Jm⁻², $\varepsilon = 1$ %, $\varphi = 70.5^\circ$, and $k_T = 3400$ MPa nm^{-1/2} in Eq. 6, the estimated value of the modified σ_{CLS} for both multilayer films are shown in Table 1. For comparison, the flow stress obtained ($\sigma_{Expt.} = H/2.7$) from the experiment is also presented in Table 1. The results in Table 1 confirm that the modified CLS model fits well with our experimental measurements. Niu *et al.* [28] have reported that the decrease in the twin density, as well as the decrease in twin thickness with a decrease in layer thickness, leads to an increase in the flow strength of the multilayer films. In the present investigation, although the 5 nm multilayer film doesn't have any signs of twin formation, the interface effect due to lower layer thickness dominates the twin effect, which ultimately leads to higher strength in case of 5 nm multilayer film.

Niu *et al.* [28] have modified the mechanistic model developed by Gu and Duo *et al.* [57,58] and Asaro and Suresh [59], referred to here as the GDAS model, to quantify the

thickness-dependent flow stress and strain-rate sensitivity by considering the nanotwin formation in nanocrystalline multilayer films. According to their model, considering the Cu phase in the multilayer films, the flow stress is assumed to be controlled by emission of partial dislocations from the interface (τ_L) and TBs (τ_{TB}) according to:

$$\frac{\tau_L}{\mu_{Cu}} = \frac{\Omega}{\mu_{Cu}b} + \left(\frac{1}{3} - \frac{1}{12\pi\beta}\right) \frac{b}{h_{Cu}} + \frac{F}{h_{Cu}} \quad (6a)$$

$$\frac{\tau_{TB}}{\mu_{Cu}} = \frac{\Gamma}{\mu_{Cu}b} + \frac{1}{2} \left(\frac{1}{3} - \frac{1}{12\pi\beta_1}\right) \frac{b}{h_{Cu}} + \frac{1}{2} \left(\frac{1}{3} - \frac{1}{12\pi\beta_2}\right) \frac{b}{\lambda} + \frac{F}{h_{Cu}} \quad (6b)$$

where, β , β_1 , and β_2 are parameters related to the extension of the non-uniform partial dislocations from the GB and the TBs. These extension parameters are related to the geometrical lengths, layer thickness (h) and twin thickness (λ), as is the flow stress [57,58]. By considering the Hall-Petch relation for the layer thickness and twin boundary through $\tau = k_0 + k_1\lambda^{-0.5} + k_1h_{Cu}^{-0.5}$, simplified versions of β , β_1 , and β_2 are:

$$\beta = \frac{1}{4\pi} \frac{1}{1-3\frac{k_1}{G\sqrt{b}}\sqrt{\frac{h_{Cu}}{b}}}; \quad \beta_1 = \frac{1}{4\pi} \frac{1}{1-6\frac{k_1}{G\sqrt{b}}\sqrt{\frac{\lambda}{b}}}; \quad \beta_2 = \frac{1}{4\pi} \frac{1}{1-6\frac{k_1}{G\sqrt{b}}\sqrt{\frac{h_{Cu}}{b}}} \quad (7)$$

Note that Eq. (6a) assumes the partial dislocation emission from the interface, and Eq. (6b) considers the emission of partial dislocations not only from the GBs, but also from the TBs. However, only τ_L is considered for 5 nm multilayer film from Eq. (6a), as the effect of nanotwins has been neglected. Further, the first term in Eq. (6a) mainly comes from the contribution of incoherent interfaces, and therefore, the parameter Ω in Eq. (6a) is defined as the critical energy needed to nucleate partials from incoherent interfaces. The value of Ω ranges between 0.02-1 J/m², as determined by atomistic simulations [58]. However, the first term in Eq. (6b) is related to the stacking fault energy (Γ). Thus, the total flow stress, τ can be obtained by considering the nanotwin wt. %:

$$\tau = \left(1 - \frac{N_T}{100}\right) \tau_L + \left(\frac{N_T}{100}\right) \tau_{TB} \quad (8)$$

The value of the flow stress estimated using the GDAS model for the 100 nm and 5 nm Cu/Mo multilayer films is presented in Table 1. Table 1 confirm that the flow stress calculated from both the modified models agree well with our experimental results after considering the nanotwin formation in the multilayer films.

The GDAS model can further be extended to calculate the thickness-dependence of m of the multilayer films. The original model was used to quantify m of nanocrystalline Cu. In the present investigation, we use this model to calculate m of the 5 nm and 100 nm single Cu layer (m_{Cu}). In the modified GDAS model, the critical dislocation half-circular loop size for activation (r_c) in the Cu phase is given from Ref. [57] as :

$$r_L^c = k \left(\frac{\tau_L}{\mu_{Cu}} \right)^{-1} b \left(\ln \frac{\sqrt{3}r_L^c}{b} + 1 \right) \quad (9a)$$

$$r_{TB}^c = k \left(\frac{\tau_{TB}}{\mu_{Cu}} \right)^{-1} b \left(\ln \frac{\sqrt{3}r_{TB}^c}{b} + 1 \right) \quad (9b)$$

In the above equations, $k=5/(16\sqrt{3}\pi)$, so the strain-rate sensitivity of the Cu, m_{Cu} , which is related to the dislocation interaction with the interface (m_{Cu}^L) and the TB (m_{Cu}^{TB}), can be calculated as:

$$m_{Cu}^L = \left(\frac{2\sqrt{3}kT}{M\pi(r_L^c)^2 b \tau_L} \right) \quad (10a)$$

$$m_{Cu}^{TB} = \left(\frac{2\sqrt{3}kT}{M\pi(r_{TB}^c)^2 b \tau_{TB}} \right) \quad (10b)$$

Finally, m_{Cu} can be estimated by using Eq. (10a) and (10b) as

$$m_{Cu} = \left(1 - \frac{N_T}{100} \right) m_{Cu}^L + \left(\frac{N_T}{100} \right) m_{Cu}^{TB} \quad (11)$$

However, for the 5 nm multilayer film, only Eq. (10a) has been used to estimate the total value of m_{Cu} . Hence, m_{Cu} calculated from Eq. 11 is presented in Table 1, which shows that the strain-rate sensitivity of Cu decreases with reducing layer thickness when the contribution from the nanotwin is considered for the case of the 100 nm multilayer film. Then, the overall strain-rate sensitivity of the multilayer film is determined by taking m_{Cu} and m_{Mo} into consideration yielding:

$$m = \left(\frac{h_{Cu}}{h_{Cu}+h_{Mo}} \right) m_{Cu} + \left(\frac{h_{Mo}}{h_{Cu}+h_{Mo}} \right) m_{Mo} \quad (12)$$

For simplicity, the above equation has been used by varying the m_{Cu} and keeping constant the value of m_{Mo} (m obtained from the experiment). Hence, the theoretical estimation of m by considering nanotwin formation in the Cu layer of the 100 nm multilayer film closely matches our experimental value. On the other hand, the calculation for the Cu layer for 5 nm multilayer film leads to a larger value of m than that of 100 nm multilayer film. Such an increasing trend of m is in broad agreement with the earlier investigation by Niu *et al.* [28], who have reported that the decrease in the twin density with the layer thickness decreases m from 0.025 for the 100 nm layer thickness to 0.015 for the 25 nm layer thickness in case of Cu/X (X=Cr, Zr) multilayer films. However, m increases sharply from 0.015 at 25 nm layer thickness to 0.035 at 5 nm layer thickness [28]. The rise in the value of strain rate sensitivity in the present investigation through the theoretical calculation is exactly opposite to our experimental observations (Table 1). This anomaly may be related to the change in deformation mechanism from the Hall-Petch relation at 100 nm multilayer film to

dislocations crossing the interface for the 5 nm multilayer film. Further, the presence of shear bands in case of 5 nm multilayer films may also be responsible for the decrease in m for the overall film.

Table 1: Summary of estimation of N_T , λ , $\sigma_{EXPT.}$, Modified σ_{CLS} , σ (GDAS model), m_{Cu} , m , and m (Expt.) for different multilayer films.

Multilayer films	N_T (%)	λ (nm)	$\sigma_{EXPT.}$	Modified σ_{CLS} (Eq. 5)	GDAS model σ (Eq. 8)	SRS m_{Cu} (Eq. 11)	SRS m (Eq. 12)	SRS (Expt.)
100 nm	35	7	3.12	3.92	4.23	0.026	0.023	0.0206
5 nm	-	-	3.55	4.06	4.92	0.031	0.031	0.0186

5. Conclusions:

The strain rate-dependent indentation response of sputter-deposited single-layered Cu, Mo, 5 nm Cu/5 nm Mo, and 100 nm Cu/100 nm Mo multilayer films having a total film thickness of 5 μm were examined by nanoindentation experiments and transmission electron microscopy of deformation microstructures. The deformation mechanisms in the single-layered, as well as multilayer films, were analyzed by correlating the strain-rate sensitivity with the defect microstructure of the films. The following conclusions are inferred from the observations:

- (1) All the films exhibit a positive value of strain-rate sensitivity. The strain-rate sensitivity of the single-layered Cu and Mo films fairly agrees with the literature for grain sizes in the micrometer range. In the case of single-layered films, high density of dislocation networks inside the grain, as well as an interaction with the neighbouring grains, were observed after indentation. The dislocation density in the indented plastic zone was found to decrease with increasing distance from the indent tip.
- (2) The evolution of shear bands in 5 nm multilayer films seems to emanate at an inclined angle with respect to the indented surface. The layers inside the shear bands are observed to be severely bent and thinned down. The size of the shear band in the 5 nm multilayer film is found to be larger for the 10^2 s^{-1} indent. On the other hand, no shear bands are observed for the 100 nm multilayer film suggesting different deformation mechanisms operate. In both multilayer films, the layers below the indent impression show a severe drop in the thickness, whereas the reduction in thickness decreases away from the indented surface. Consistently,

the true compressive plastic strain calculated in the thickness direction is found to decrease with the distance from the indentation surface for all the multilayer films. In case of 100 nm Cu/100 nm Mo multilayer films, the true compressive plastic strain is found to decrease from 51.2 % and 20 % in the first layer to 10 % and 4 % in the fourth layer for the Cu and Mo layers, respectively. Further, material pile-up in the first layer of Cu around the indent impression was observed in the 100 nm multilayer film, which leads to a larger value of true plastic strain in the first layer of Cu (i.e. 51.2 %).

- (3) The strain-rate sensitivity of the 5 nm Cu/Mo multilayer film is lower than that of the 100 nm film. The strengthening mechanism has been discussed by considering the influences of the layer thickness of the films. The reduction in strain-rate sensitivity is closely related to the evolution of shear bands as well as an absence of growth nanotwin formation for the 5 nm multilayer film. A modified CLS model has been used to estimate the flow strength and the strain-rate sensitivity in a manner that considers the contribution from the layer thickness, as well as nanotwin formation in 100 nm multilayer film, which complement our experimental observation.

Acknowledgement:

WHH, GMP, and AM acknowledge funding from the Center for Research Excellence on Dynamically Deformed Solids (CREDDS) sponsored by the Department of Energy – National Nuclear Security Administration (DOE-NNSA), Stewardship Science Academic Program under the Award No. DE-NA0003857. BPS acknowledges support from University of Michigan. Electron microscopy was performed at the Michigan Center for Materials Characterization.

References:

- [1] S. Wei, S. Zheng, L. Zhang, Y. Liu, J. Wang, X. Wang, J. Wang, Role of interfacial transition zones in the fracture of Cu/V nanolamellar multilayers, *Mater. Res. Lett.* 8 (2020) 299–306. <https://doi.org/10.1080/21663831.2020.1755379>.
- [2] M.J. Demkowicz, I.J. Beyerlein, The effects of nanoscale confinement on the behavior of metal laminates, *Scr. Mater.* 187 (2020) 130–136. <https://doi.org/10.1016/j.scriptamat.2020.05.057>.
- [3] Y.F. Zhao, Y.Q. Wang, K. Wu, J.Y. Zhang, G. Liu, J. Sun, Unique mechanical properties of Cu/(NbMoTaW) nanolaminates, *Scr. Mater.* 154 (2018) 154–158. <https://doi.org/10.1016/j.scriptamat.2018.05.042>.

- [4] M. Nasim, Y. Li, M. Dargusch, C. Wen, Ultra-strong and ductile Ta/Co nanolaminates strengthened via grain-boundary expanding and interfacial sliding, *Appl. Mater. Today*. 23 (2021) 100983. <https://doi.org/10.1016/j.apmt.2021.100983>.
- [5] Y.P. Li, J. Tan, G.P. Zhang, Interface instability within shear bands in nanoscale Au/Cu multilayers, *Scr. Mater.* 59 (2008) 1226–1229. <https://doi.org/10.1016/j.scriptamat.2008.08.017>.
- [6] F. Wang, P. Huang, M. Xu, T.J. Lu, K.W. Xu, Shear banding deformation in Cu/Ta nano-multilayers, *Mater. Sci. Eng. A*. 528 (2011) 7290–7294. <https://doi.org/10.1016/j.msea.2011.06.019>.
- [7] C.R. Mayer, L.W. Yang, S.S. Singh, J. Llorca, J.M. Molina-Aldareguia, Y.L. Shen, N. Chawla, Anisotropy, size, and aspect ratio effects on micropillar compression of Al-SiC nanolaminate composites, *Acta Mater.* 114 (2016) 25–32. <https://doi.org/10.1016/j.actamat.2016.05.018>.
- [8] A. Kelling, K.R. Mangipudi, I. Knorr, T. Liese, H.U. Krebs, C.A. Volkert, Investigating fracture of nanoscale metal-ceramic multilayers in the transmission electron microscope, *Scr. Mater.* 115 (2016) 42–45. <https://doi.org/10.1016/j.scriptamat.2015.12.026>.
- [9] P.L. Sun, J.P. Chu, T.Y. Lin, Y.L. Shen, N. Chawla, Characterization of nanoindentation damage in metal/ceramic multilayered films by transmission electron microscopy (TEM), *Mater. Sci. Eng. A*. 527 (2010) 2985–2992. <https://doi.org/10.1016/j.msea.2010.01.040>.
- [10] D. Bhattacharyya, N.A. Mara, P. Dickerson, R.G. Hoagland, A. Misra, A transmission electron microscopy study of the deformation behavior underneath nanoindents in nanoscale Al-TiN multilayered composites, *Philos. Mag.* 90 (2010) 1711–1724. <https://doi.org/10.1080/14786430903459691>.
- [11] J.Y. Zhang, G. Liu, J. Sun, Self-toughening crystalline Cu/amorphous Cu-Zr nanolaminates: Deformation-induced devitrification, *Acta Mater.* 66 (2014) 22–31. <https://doi.org/10.1016/j.actamat.2013.11.061>.
- [12] W. Guo, E. Jäggle, J. Yao, V. Maier, S. Korte-Kerzel, J.M. Schneider, D. Raabe, Intrinsic and extrinsic size effects in the deformation of amorphous

- CuZr/nanocrystalline Cu nanolaminates, *Acta Mater.* 80 (2014) 94–106.
<https://doi.org/10.1016/j.actamat.2014.07.027>.
- [13] Y. Cui, O.T. Abad, F. Wang, P. Huang, T.J. Lu, K.W. Xu, J. Wang, Plastic deformation modes of CuZr/Cu Multilayers, *Sci. Rep.* 6 (2016) 2–7.
<https://doi.org/10.1038/srep23306>.
- [14] I. Knorr, N.M. Cordero, E.T. Lilleodden, C.A. Volkert, Mechanical behavior of nanoscale Cu/PdSi multilayers, *Acta Mater.* 61 (2013) 4984–4995.
<https://doi.org/10.1016/j.actamat.2013.04.047>.
- [15] V. Maier-Kiener, K. Durst, Advanced nanoindentation testing for studying strain-rate sensitivity and activation volume, *JOM.* 69 (2017) 2246–2255.
<https://doi.org/10.1007/s11837-017-2536-y>.
- [16] R. Schwaiger, B. Moser, M. Dao, N. Chollacoop, S. Suresh, Some critical experiments on the strain-rate sensitivity of nanocrystalline nickel, *Acta Mater.* 51 (2003) 5159–5172. [https://doi.org/10.1016/S1359-6454\(03\)00365-3](https://doi.org/10.1016/S1359-6454(03)00365-3).
- [17] L. Lu, T. Zhu, Y. Shen, M. Dao, K. Lu, S. Suresh, Stress relaxation and the structure size-dependence of plastic deformation in nanotwinned copper, *Acta Mater.* 57 (2009) 5165–5173. <https://doi.org/10.1016/j.actamat.2009.07.018>.
- [18] L. Lu, S.X. Li, K. Lu, An abnormal strain rate effect on tensile behavior in nanocrystalline copper, *Scr. Mater.* 45 (2001) 1163–1169.
[https://doi.org/10.1016/S1359-6462\(01\)01138-1](https://doi.org/10.1016/S1359-6462(01)01138-1).
- [19] L. Lu, R. Schwaiger, Z.W. Shan, M. Dao, K. Lu, S. Suresh, Nano-sized twins induce high rate sensitivity of flow stress in pure copper, *Acta Mater.* 53 (2005) 2169–2179.
<https://doi.org/10.1016/j.actamat.2005.01.031>.
- [20] Y.M. Wang, A. V. Hamza, E. Ma, Temperature-dependent strain rate sensitivity and activation volume of nanocrystalline Ni, *Acta Mater.* 54 (2006) 2715–2726.
<https://doi.org/10.1016/j.actamat.2006.02.013>.
- [21] Q. Wei, S. Cheng, K.T. Ramesh, E. Ma, Effect of nanocrystalline and ultrafine grain sizes on the strain rate sensitivity and activation volume: Fcc versus bcc metals, *Mater. Sci. Eng. A.* 381 (2004) 71–79. <https://doi.org/10.1016/j.msea.2004.03.064>.
- [22] Q. Wei, L. Kecskes, T. Jiao, K.T. Hartwig, K.T. Ramesh, E. Ma, Adiabatic shear

- banding in ultrafine-grained Fe processed by severe plastic deformation, *Acta Mater.* 52 (2004) 1859–1869. <https://doi.org/10.1016/j.actamat.2003.12.025>.
- [23] Q. Wei, T. Jiao, S.N. Mathaudhu, E. Ma, K.T. Hartwig, K.T. Ramesh, Microstructure and mechanical properties of tantalum after equal channel angular extrusion (ECAE), *Mater. Sci. Eng. A.* 358 (2003) 266–272. [https://doi.org/10.1016/S0921-5093\(03\)00305-8](https://doi.org/10.1016/S0921-5093(03)00305-8).
- [24] J.S. Carpenter, A. Misra, M.D. Uchic, P.M. Anderson, Strain rate sensitivity and activation volume of Cu/Ni metallic multilayer thin films measured via micropillar compression, *Appl. Phys. Lett.* 101 (2012). <https://doi.org/10.1063/1.4739521>.
- [25] Y. Liu, K.M. Yang, J. Hay, E.G. Fu, X. Zhang, The effect of coherent interface on strain-rate sensitivity of highly textured Cu/Ni and Cu/V multilayers, *Scr. Mater.* 162 (2019) 33–37. <https://doi.org/10.1016/j.scriptamat.2018.10.021>.
- [26] Y. Ma, G.J. Peng, Y.H. Feng, T.H. Zhang, Nanoindentation investigation on creep behavior of amorphous Cu-Zr-Al/nanocrystalline Cu nanolaminates, *J. Non-Cryst. Solids.* 465 (2017) 8–16. <https://doi.org/10.1016/j.jnoncrysol.2017.03.037>.
- [27] Q. Zhou, J.J. Li, F. Wang, P. Huang, K.W. Xu, T.J. Lu, Strain rate sensitivity of Cu/Ta multilayered films: Comparison between grain boundary and heterophase interface, *Scr. Mater.* 111 (2016) 123–126. <https://doi.org/10.1016/j.scriptamat.2015.08.031>.
- [28] J.J. Niu, J.Y. Zhang, G. Liu, P. Zhang, S.Y. Lei, G.J. Zhang, J. Sun, Size-dependent deformation mechanisms and strain-rate sensitivity in nanostructured Cu/X (X = Cr, Zr) multilayer films, *Acta Mater.* 60 (2012) 3677–3689. <https://doi.org/10.1016/j.actamat.2012.03.052>.
- [29] D. Pan, A. Inoue, T. Sakurai, M.W. Chen, Experimental characterization of shear transformation zones for plastic flow of bulk metallic glasses, *Proc. Natl. Acad. Sci.* 105 (2008) 14769–14772. <https://doi.org/10.1073/pnas.0806051105>.
- [30] D. Bhattacharyya, N.A. Mara, P. Dickerson, R.G. Hoagland, A. Misra, Transmission electron microscopy study of the deformation behavior of Cu/Nb and Cu/Ni nanoscale multilayers during nanoindentation, *J. Mater. Res.* 24 (2009) 1291–1302. <https://doi.org/10.1557/jmr.2009.0147>.
- [31] S.N. Monteiro, L.F.C. Nascimento, N.T. Simonassi, E.S. Lima, A.S. De Paula, F.O.

- De Braga, High temperature work hardening stages, dynamic strain aging and related dislocation structure in tensile deformed AISI 301 stainless steel, *J. Mater. Res. Technol.* 7 (2018) 571–577. <https://doi.org/10.1016/j.jmrt.2018.06.020>.
- [32] S.N. Monteiro, L.P. Brandão, T.G. De Sousa, F.D.C. Garcia Filho, Novel methods for dislocation density estimation in highly compacted tangles, *J. Mater. Res. Technol.* 9 (2020) 2072–2078. <https://doi.org/10.1016/j.jmrt.2019.12.040>.
- [33] Y.G. Shen, Effect of deposition conditions on mechanical stresses and microstructure of sputter-deposited molybdenum and reactively sputter-deposited molybdenum nitride films, *Mater. Sci. Eng. A.* 359 (2003) 158–167. [https://doi.org/10.1016/S0921-5093\(03\)00336-8](https://doi.org/10.1016/S0921-5093(03)00336-8).
- [34] Y. Cui, B. Derby, N. Li, N.A. Mara, A. Misra, Suppression of shear banding in high-strength Cu/Mo nanocomposites with hierarchical bicontinuous intertwined structures, *Mater. Res. Lett.* 6 (2018) 184–190. <https://doi.org/10.1080/21663831.2018.1431315>.
- [35] X. Zhang, O. Anderoglu, A. Misra, H. Wang, Influence of deposition rate on the formation of growth twins in sputter-deposited 330 austenitic stainless steel films, *Appl. Phys. Lett.* 90 (2007) 2005–2008. <https://doi.org/10.1063/1.2720708>.
- [36] O. Anderoglu, A. Misra, H. Wang, X. Zhang, Thermal stability of sputtered Cu films with nanoscale growth twins, *J. Appl. Phys.* 103 (2008). <https://doi.org/10.1063/1.2913322>.
- [37] M. Rester, C. Motz, R. Pippin, Microstructural investigation of the volume beneath nanoindentations in copper, *Acta Mater.* 55 (2007) 6427–6435. <https://doi.org/10.1016/j.actamat.2007.08.001>.
- [38] J. Chen, L. Lu, K. Lu, Hardness and strain rate sensitivity of nanocrystalline Cu, *Scr. Mater.* 54 (2006) 1913–1918. <https://doi.org/10.1016/j.scriptamat.2006.02.022>.
- [39] J. Zhao, P. Huang, K.W. Xu, F. Wang, T.J. Lu, Indentation size and loading strain rate dependent creep deformation of nanocrystalline Mo, *Thin Solid Films.* 653 (2018) 365–370. <https://doi.org/10.1016/j.tsf.2018.03.068>.
- [40] B.K. Derby, A. Chatterjee, A. Misra, Metal-ion-controlled growth and nanoindentation response of 3D, bicontinuous Cu-Fe thin films, *J. Appl. Phys.* 128 (2020). <https://doi.org/10.1063/5.0014441>.

- [41] A. Misra, M. Verdier, Y.C. Lu, H. Kung, T.E. Mitchell, M. Nastasi, J.D. Embury, Structure and mechanical properties of Cu-X (X = Nb,Cr,Ni) nanolayered composites, *Scr. Mater.* 39 (1998) 555–560. [https://doi.org/10.1016/S1359-6462\(98\)00196-1](https://doi.org/10.1016/S1359-6462(98)00196-1).
- [42] S.R. Jian, Y.Y. Lin, Berkovich nanoindentation-induced dislocation energetics and pop-in effects in ZnSe thin films, *J. Alloys Compd.* 590 (2014) 153–156. <https://doi.org/10.1016/j.jallcom.2013.12.103>.
- [43] R.P. Carreker, W.R. Hibbard, Tensile deformation of high-purity copper as a function of temperature, strain rate, and grain size, *Acta Metall.* 1 (1953). [https://doi.org/10.1016/0001-6160\(53\)90022-4](https://doi.org/10.1016/0001-6160(53)90022-4).
- [44] J. Zhao, P. Huang, K.W. Xu, F. Wang, T.J. Lu, Indentation size and loading strain rate dependent creep deformation of nanocrystalline Mo, *Thin Solid Films.* 653 (2018) 365–370. <https://doi.org/10.1016/j.tsf.2018.03.068>.
- [45] J. Zhao, F. Wang, P. Huang, T.J. Lu, K.W. Xu, Depth dependent strain rate sensitivity and inverse indentation size effect of hardness in body-centered cubic nanocrystalline metals, *Mater. Sci. Eng. A.* 615 (2014) 87–91. <https://doi.org/10.1016/j.msea.2014.07.057>.
- [46] Q. Wei, Strain rate effects in the ultrafine grain and nanocrystalline regimes-influence on some constitutive responses, *J. Mater. Sci.* 42 (2007) 1709–1727. <https://doi.org/10.1007/s10853-006-0700-9>.
- [47] G.T. Gray, P.S. Follansbee, C.E. Frantz, Effect of residual strain on the substructure development and mechanical response of shock-loaded copper, *Mater. Sci. Eng. A.* 111 (1989) 9–16. [https://doi.org/10.1016/0921-5093\(89\)90192-5](https://doi.org/10.1016/0921-5093(89)90192-5).
- [48] S.P. Wen, R.L. Zong, F. Zeng, Y. Gao, F. Pan, Nanoindentation investigation of the mechanical behaviors of nanoscale Ag/Cu multilayers, *J. Mater. Res.* 22 (2007) 3423–3431. <https://doi.org/10.1557/jmr.2007.0423>.
- [49] A. Misra, J.P. Hirth, R.G. Hoagland, Length-scale-dependent deformation mechanisms in incoherent metallic multilayered composites, *Acta Mater.* 53 (2005) 4817–4824. <https://doi.org/10.1016/j.actamat.2005.06.025>.
- [50] J.Y. Xie, P. Huang, F. Wang, Y. Li, L.F. Zhang, K.W. Xu, Strain rate dependent shear banding deformation in Al/W nanomultilayers, *Integr. Ferroelectr.* 146 (2013) 168–176.

- <https://doi.org/10.1080/10584587.2013.790247>.
- [51] J.Y. Zhang, G. Liu, R.H. Wang, J. Li, J. Sun, E. Ma, Double-inverse grain size dependence of deformation twinning in nanocrystalline Cu, *Phys. Rev. B - Condens. Matter Mater. Phys.* 81 (2010) 2–5. <https://doi.org/10.1103/PhysRevB.81.172104>.
- [52] Y. Wei, A.F. Bower, H. Gao, Enhanced strain-rate sensitivity in fcc nanocrystals due to grain-boundary diffusion and sliding, *Acta Mater.* 56 (2008) 1741–1752. <https://doi.org/10.1016/j.actamat.2007.12.028>.
- [53] C.A. Schuh, T.C. Hufnagel, U. Ramamurty, Mechanical behavior of amorphous alloys, *Acta Mater.* 55 (2007) 4067–4109. <https://doi.org/10.1016/j.actamat.2007.01.052>.
- [54] B.P. Sahu, A. Dutta, R. Mitra, Influence of Composition on Nanoindentation Response of Ni-Zr Alloy Thin Films, *Metall. Mater. Trans. A Phys. Metall. Mater. Sci.* 50 (2019). <https://doi.org/10.1007/s11661-019-05467-8>.
- [55] B.P. Sahu, A. Dutta, R. Mitra, Mechanism of negative strain rate sensitivity in metallic glass film, *J. Alloys Compd.* 784 (2019). <https://doi.org/10.1016/j.jallcom.2019.01.024>.
- [56] A. Bhattacharyya, G. Singh, K. Eswar Prasad, R. Narasimhan, U. Ramamurty, On the strain rate sensitivity of plastic flow in metallic glasses, *Mater. Sci. Eng. A.* 625 (2015) 245–251. <https://doi.org/10.1016/j.msea.2014.12.004>.
- [57] P. Gu, M. Dao, R.J. Asaro, S. Suresh, A unified mechanistic model for size-dependent deformation in nanocrystalline and nanotwinned metals, *Acta Mater.* 59 (2011) 6861–6868. <https://doi.org/10.1016/j.actamat.2011.07.019>.
- [58] P. Gu, B.K. Kad, M. Dao, A modified model for deformation via partial dislocations and stacking faults at the nanoscale, *Scr. Mater.* 62 (2010) 361–364. <https://doi.org/10.1016/j.scriptamat.2009.10.035>.
- [59] R.J. Asaro, S. Suresh, Mechanistic models for the activation volume and rate sensitivity in metals with nanocrystalline grains and nano-scale twins, *Acta Mater.* 53 (2005) 3369–3382. <https://doi.org/10.1016/j.actamat.2005.03.047>.